Error Analysis of Bulk-Density Measurements for Metal-Type DebriSat Fragments

Cesar Carrasquilla, Matthew Biles, Norman Fitz-Coy
Department of Mechanical & Aerospace Engineering, The University of Florida

ABSTRACT

DebriSat is a collaborative effort between NASA, The Space Force Space Systems Command (SSC), the Aerospace Corporation, and the University of Florida aimed at updating the satellite breakup model by conducting a catastrophic collision using a 56 kg representative satellite constructed with modern techniques and materials. The project involves the collection of the resulting debris, termed fragments, and their characterization based on physical properties such as shape and material, and size measurements which include dimensional lengths, characteristic length, average cross-sectional area, volume, density, and area to mass ratio. A specialized imaging system, referred to as the 3D Imager, was developed for the purpose of producing these size measurements. The system produces 3D models of the fragments and has been employed to characterize over 3,000 debris pieces with at least one physical dimension larger than 3 mm. Previous estimations of volume error were obtained using a limited selection of well-defined calibration objects. Under ideal conditions, the error distribution would remain consistent across different fragment shapes. However, the algorithm generating the 3D geometry introduces a systematic bias in volume computation. Given that the calibration objects do not accurately represent the physical characteristics of the fragments in the dataset, it becomes necessary to accurately characterize these errors. In this study, we provide an overview of the identified sources of error within the system and leverage the known densities of the materials for aluminum and stainless-steel fragments to provide a more accurate characterization of the errors in volume and density measurements produced by the 3D imager system.

1. INTRODUCTION

The DebriSat project was established to design and build a modern satellite mock-up representative of current low Earth orbit (LEO) satellites, and to conduct a hypervelocity impact test to simulate a catastrophic breakup event. The objective was to collect, measure, and characterize the resulting fragments, of size 2 mm and larger, to improve existing satellite breakup models used by NASA and the Department of Defense (DOD) [1-5]. Initially, it was predicted that the hypervelocity impact test performed on DebriSat would produce 85,000 fragments; however, as of July 2024, 294,501 fragments have been collected and 217,648 fragments have been recorded [1-3]. This drastic underestimation further illustrates the importance of updating satellite breakup models representative of modern materials.

Characterizing DebriSat fragments and recording the volume and density is crucial for the accuracy of breakup model simulations. Specifically, this data enables calculations such as the dynamics of debris, various aerodynamic and ballistic properties, and accurate area-to-mass (A/M) ratios [4]. These calculations are essential for predicting and simulating debris trajectories and the lifespan of fragments as they decay due to atmospheric drag. This paper's statistical analysis can enhance the understanding of debris cloud distributions and their respective fragments' volumes and densities resulting from catastrophic breakups in low Earth orbit. This is crucial for predicting the spatial and temporal evolution of debris fields following a breakup event, which directly impacts collision avoidance strategies, debris mitigation efforts, and the design of future satellites.

This paper aims to analyze the errors in bulk-density measurements of metal-type fragments produced by the DebriSat project. It aims to identify and characterize the sources of error in the 3D imaging system used for fragment analysis, particularly focusing on how these errors affect volume and density calculations. The 3D imaging system is comprised of six cameras and a platform that rotates, capturing images of all angles of the desired fragment [1-3, 5]. The captured images create a 3D model through a subtractive space carving algorithm. The study provides insight, through statistical analysis, into the systematic biases introduced by the 3D imaging system.

Prior work on error analysis of the 3D imaging system focused on using calibration objects with known dimensions to establish error bounds; however, these objects are not representative of the various geometries and surface features found in DebriSat fragments. For instance, calibration objects are convex and easily distinguishable from their backgrounds, facilitating accurate image segmentation. Real-world observations suggest that factors like surface specularity, geometry, cast shadows, presence of dust, and calibration inaccuracies influence the resulting 3D models of imaged fragments — potentially overshadowing the well-known limitations of the space-carving algorithm, which is assumed to be the dominant source of error. This document aims to illustrate how these sources of errors propagate through the system by characterizing the density bias introduced when modeling metal fragments, specifically focusing on aluminum (AL), and stainless steel (SS).

Hereafter, unless otherwise specified, any references to an increase or decrease in each quantity refers to the change between the value computed from the 3D model and that quantity's actual value. For example, a “3% increase in volume” implies that the volume calculated from the 3D model is 3% greater than the true volume of the object being imaged.

2. DEBRISAT 3D IMAGING SYSTEM

The DebriSat 3D imaging system uses a subtractive space-carving algorithm to create 3D models of fragments (i.e., the object is assumed to occupy a predefined volumetric grid, then voxels are removed iteratively to achieve consistency with input images). The principal drawback of the algorithm is that it does not always reproduce concavities and curved surfaces accurately [6]. Consequently, the process incorrectly estimates the true volume of concave objects systematically. If an object is solid and has a homogeneous composition, its true volume can be computed using its density and mass. Alternatively, the density computed from the 3D model can be considered an estimate of the object's true density. By examining the distribution of these density estimates, we can gain insights into how this systematic bias affects the results. For these investigations, metal-type fragments are particularly suitable because there are sufficient samples as single-material fragments, and their uniform composition makes their volume readily computable.

2.1 Error sources

The system follows a sequential workflow that encompasses multiple phases: camera calibration, image acquisition, image segmentation, space-carving, and meshing. Errors introduced in the early stages of the process compound, leading to inaccuracies in the final 3D model. These errors can be classified into three main types: calibration errors, segmentation errors, and algorithmic errors.

2.1.1 Calibration errors

Calibration is the determination of the spatial position, orientation, and internal camera parameters that influence how a 3D scene is mapped onto a 2D image. This process dictates the trajectory of the carving rays during space carving. Deviations in calibration alter the model's boundaries (Fig. 1) and typically decrease the volume due to the removal of occupied voxels (Fig. 2).

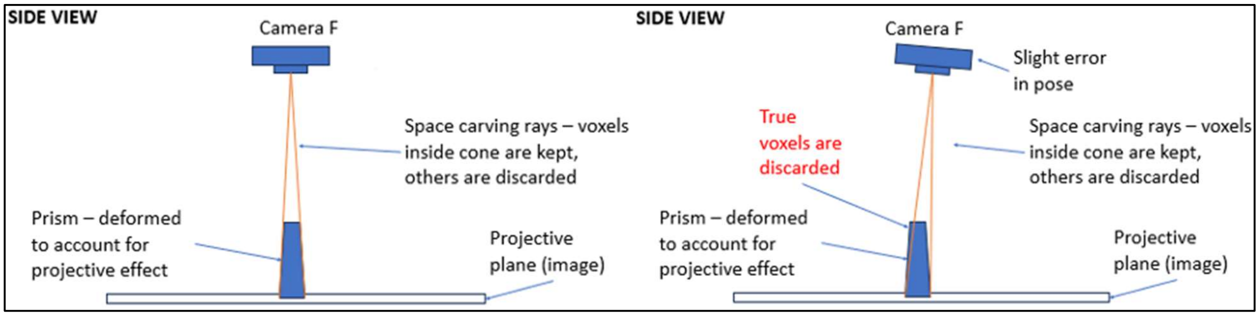

Fig. 1: Illustration showing the effects of a hypothetical deviation in the camera pose

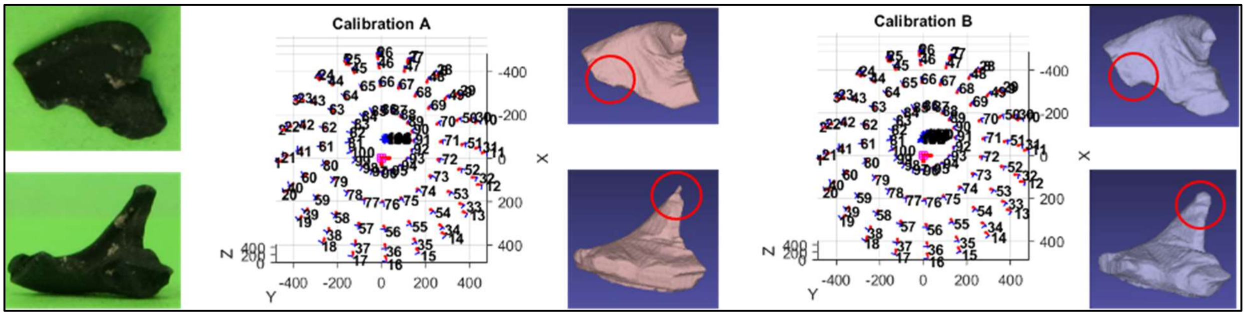

Fig. 2: Effects of different calibrations on the same fragment

2.1.2 Segmentation errors

Segmentation refers to the act of partitioning images into foreground and background pixels. These classifications are used as predicates to determine consistency between voxels and images.

Misclassified background pixels cause the removal of genuine object volume (false-negative voxels), while misclassified foreground pixels (e.g.: shadows, foam) can lead to an increase in volume (false-positive voxels). Segmentation is heavily dependent on the surface appearance of the fragment and illumination conditions in the scene. Reflective surfaces may blend into the background when viewed at certain angles, causing perforations that reduce the volume. Shadows can closely resemble green-tinted areas on a smaller scale, causing the addition of volume that does not belong to the fragment or removal of true-positive voxels. Examples of both types of misclassified pixels can be seen in Fig. 3.

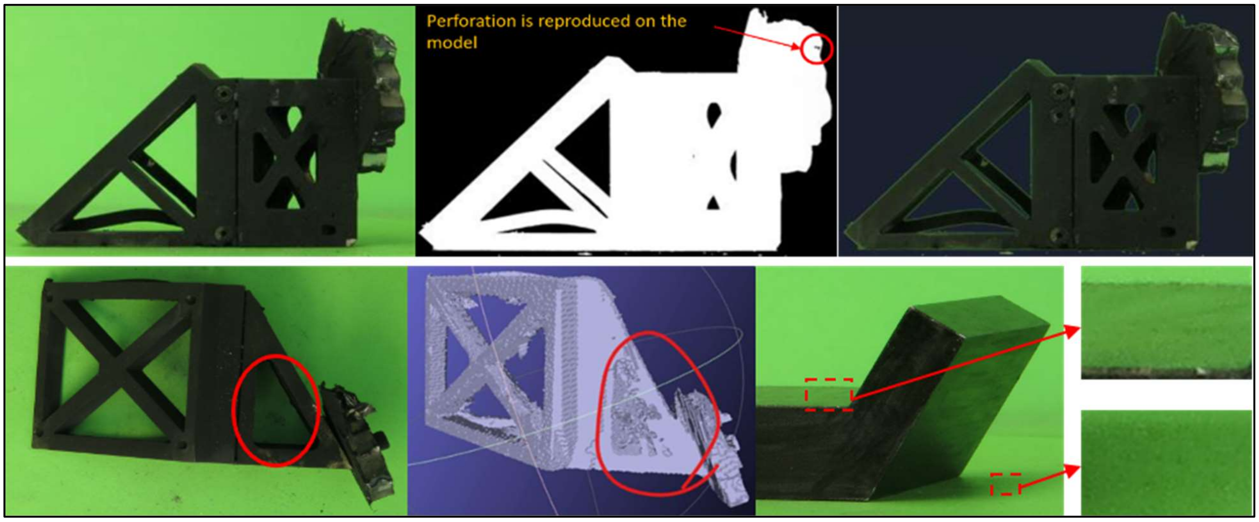

Fig. 3: Effect of specular surfaces on segmented image (top); effect of shadows on space-carved object (bottom)

2.1.3 Algorithmic errors

The space-carving process reconstructs a shape, known as the visual hull, from a set of silhouettes captured at known locations [7]. However, this reconstruction process has several limitations. Certain concavities cannot be reproduced [6]. Previous studies have shown that when the object imaged is convex and non-specular, the volume error is less than 1% [8, 9], however, most metal-type fragments exhibit concavities that are not reproducible. Additionally, the discretized selection of observation viewpoints impedes the ability to capture smooth, curved surfaces and flat surfaces not parallel to carving rays (Fig. 4). Voxels that are not carved are assumed to be occupied by the fragment and used to generate the mesh that becomes the 3D model. Assuming correctly segmented silhouettes and accurate camera positioning, the actual volume occupied by the object is fully contained within the visual hull. Consequently, since the volume is derived from the visual hull, the true volume tends to be overestimated.

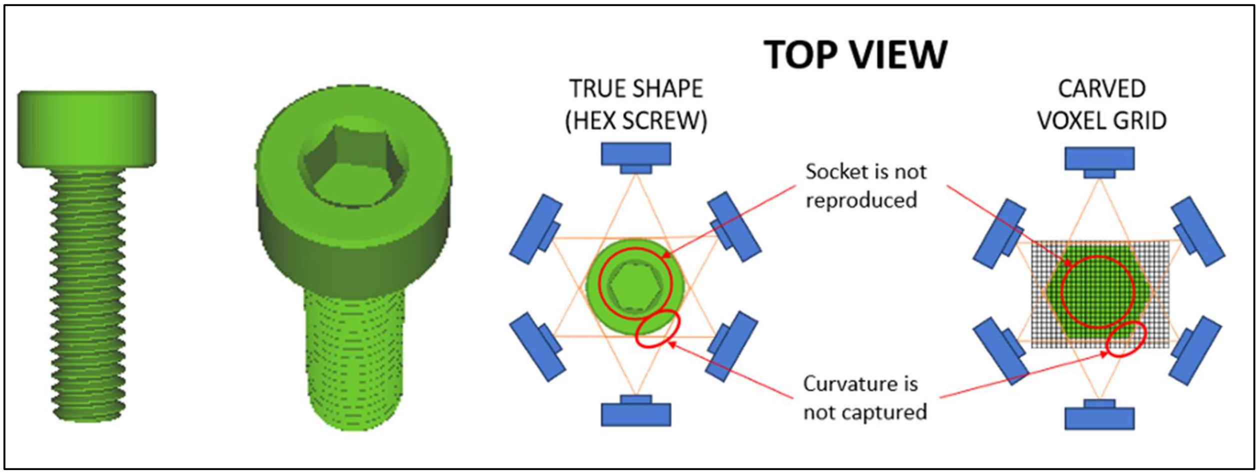

Fig. 4: Illustration showing the limitation of space-carving a hexagonal screw

3. METHODOLOGY

DebriSat fragments imaged with the 3D imaging system were analyzed, focusing specifically on those with primary materials categorized as METAL, AL, or SS. Titanium (TI) data has been excluded from this study due to all TI fragments having been found and insufficient data to make any statistical conclusions. Data attributes such as mass, density, and volume were extracted from the most recent revision for each fragment. Fragments composed of multiple materials, indicated by having a secondary material other than 'NONE,' were omitted from the study. The selected fragments were then grouped based on their primary material for further analysis. Outliers from each group were identified and removed by using the scaled median absolute deviation method implemented in MATLAB. Statistical tests for normality and graphical techniques were employed to assess the distribution of density values for AL and SS fragments. A subset of AL fragments, selected randomly (but exhibiting underestimated volumes), were manually inspected and categorized based on the most probable causes for the underestimation.

To streamline the analysis, the assumption that errors in mass measurements are negligible is accepted. The relative volume error is computed using the following formula:

$$V_{true} = V_{computed} * \frac{\rho_{computed}}{\rho_{true}} \tag{1}$$

$$relative\ error = \frac{V_{computed} - V_{true}}{V_{true}} = \frac{V_{computed}}{V_{true}} - 1 = \frac{\rho_{true}}{\rho_{computed}} - 1 \tag{2}$$

The histograms of the relative errors are presented together with the 90% and 95% coverage intervals. The results are shown in Tables 1-3.

3.1 Fragment Shape Characterization

Through the DebriSat assessment process, fragments are characterized based on their shapes [1-5]. The process and various characterizations are shown in Fig. 5 and Fig. 6.

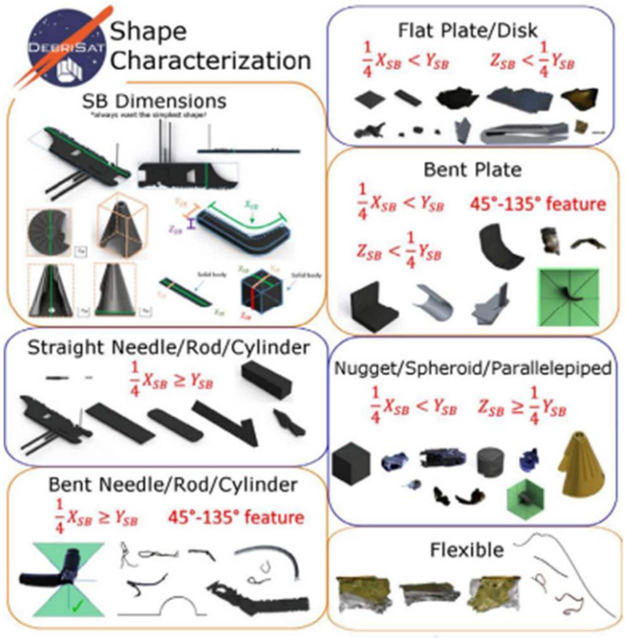

Fig. 5: Diagram of shape characterizations [1].

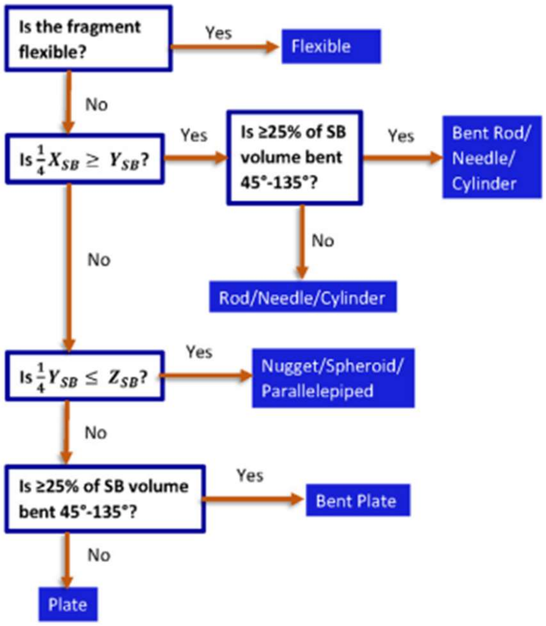

Fig. 6: Process map of characterizing fragments [1].

3.2 Statistical Analysis Background Research

For this study, thorough background research in normality assessment was conducted. Outlined below is a summary of the information collected that guided the normality assessment procedure.

As concluded in [10], the power rankings of statistical tests for data sets of our size are as follows: the Shapiro-Wilk test, the Kolmogorov-Smirnov test, the Lilliefors test, and lastly the Anderson-Darling test. The Cramer-Von Mises test was not discussed as more or less powerful than any given test in [10]. The Anderson-Darling and Kolmogorov-Smirnov tests differ slightly from the Cramer-Von Mises test, each emphasizing distinct aspects of a distribution. The Anderson-Darling test gives more weight to the tails of a distribution, while the Kolmogorov-Smirnov test gives more weight to the central part of the distribution, and the Cramer-Von Mises test lies in between the two [10, 11]. Finally, it is important to note that sample size significantly affects the accuracy of normality tests. As per [10], no normality test is reliable for sample sizes smaller than 30.

When statistically analyzing a given data set for normality, normality tests are useful, but graphical analysis methods can further support or disprove a conclusion. Not only can Q-Q plots aid in the conclusion of a distribution, but [11] places more significance on Q-Q plots than classic normality tests. Q-Q plots and histograms can help visualize distributions and demonstrate kurtosis and skewness of data. Comparing and contrasting the results of normality tests with graphical analysis methods and the coefficients of kurtosis and skewness provides a solid foundation for determining a data set's distribution [10, 11].

4. RESULTS AND DISCUSSION

Table 1 shows the breakdown of the sample based on the fragment shape and material classification. The primary shape seen on the fragments corresponds to the 'Nugget' category, which makes up over 66% of the composition in all the metal categories. The "Count" column refers to the number of fragments belonging to a shape category and the "Percentage" column refers to the relative composition of each shape category within a fixed metal category. Table 2 shows the summary statistics of the density estimates, with the mean and median density of AL fragments being slightly under the density range of the AL alloys present in the satellite while in the case of SS, only the mean falls outside its corresponding range. The density ranges are based on the known densities of the different alloys classified under each metal category. It is worth noting that SS fragments exhibit a variation that is significantly higher than that of AL fragments. Finally, Table 3 shows summary statistics of the relative error in volume, with the median relative error of AL fragments being 7% while the median error of SS fragments is -8%.

Table 1: Shape Composition of Metal Fragments.

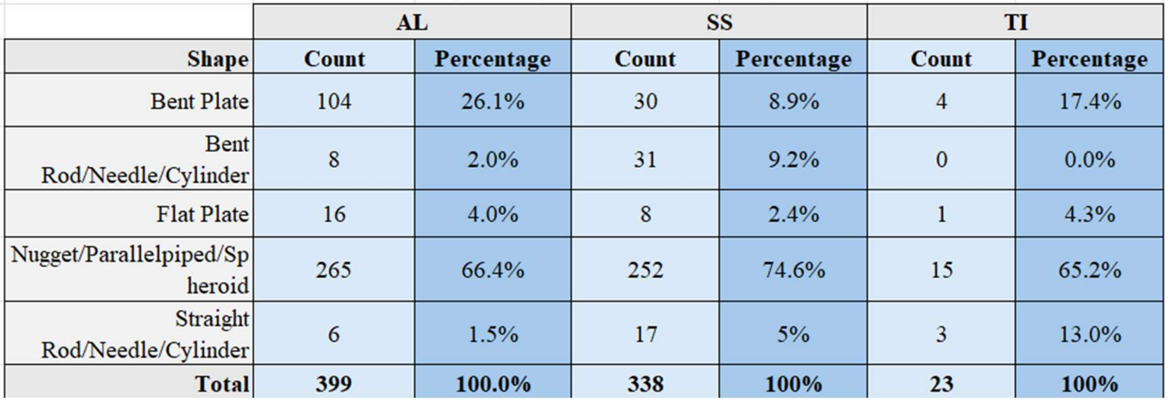

	AL		**SS**		**TI**	
Shape	**Count**	**Percentage**	**Count**	**Percentage**	**Count**	**Percentage**
Bent Plate	104	26.1%	30	8.9%	4	17.4%
Bent Rod/Needle/Cylinder	8	2.0%	31	9.2%	0	0.0%
Flat Plate	16	4.0%	8	2.4%	1	4.3%
Nugget/Parallelpiped/Spheroid	265	66.4%	252	74.6%	15	65.2%
Straight Rod/Needle/Cylinder	6	1.5%	17	5%	3	13.0%
Total	**399**	**100.0%**	**338**	**100%**	**23**	**100%**

Table 2: Statistics of AL, SS, and TI Density Distributions.

Primary Material	**Count**	**Mean density (g/cm^3)**	**Median density (g/cm^3)**	**Min density (g/cm^3)**	**Max density (g/cm^3)**	**St Dev. density (g/cm^3)**	**Density range (g/cm^3)**	**99% CI of mean (g/cm^3)**
AL	399	2.57	2.53	0.69	4.28	0.60	(2.68, 2.78)	(2.49, 2.64)
SS	338	7.77	7.97	1.08	15.10	2.52	(7.90, 8.00)	—
TI	23	4.98	4.87	4.10	6.23	0.58	(4.50, 4.50)	—

Table 3: Statistics of Percentage Error in Volume

Primary Material	Count	Mean absolute percentage error volume	Median percentage error volume	Median absolute percentage error volume	Min percentage error volume	Max percentage error volume
AL	399	23%	7%	15%	-37%	290%
SS	338	36%	-2%	19%	-48%	624%
TI	23	11%	-8%	9%	-28%	10%

The unclassified metal distribution loosely mirrors the overlaid distributions for AL, SS, and TI, particularly around the known metal densities as shown in Fig. 7. This discussion assumes that the error in mass measurements is negligible given that the balances on-site are correctly calibrated and used.

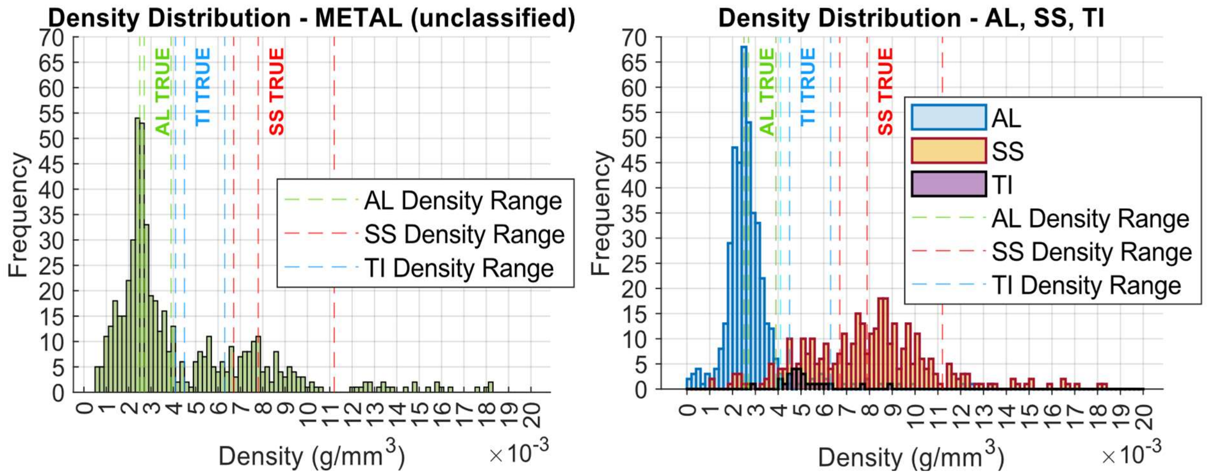

Fig. 7: Histograms of Metal densities

4.1 Statistical Analysis for Concluding a Normal Distribution

For simplification, we assume that the various density measurements follow a normal distribution. This assumption is validated by applying several normality tests, examining Q-Q plots, and visually inspecting histograms, apart from TI-labelled density measurements whose small sample size is unsuitable for analysis.

4.1.1 Assessment of Normality

Both distributions fail the Anderson-Darling and Cramer-Von Mises tests while passing the Kolmogorov-Smirnov and Shapiro-Wilk tests. First and foremost, passing the Shapiro-Wilk test provides a strong basis for concluding normality, as it is the most powerful test available [10]. The failure of the Cramer-Von Mises test implies that the Anderson-Darling test would be least applicable to AL and SS distributions, as it is a modification of the Cramer-Von Mises test. Additionally, because the Anderson-Darling test places more weight on the tails of a distribution, its results are less significant in this analysis [10, 11]. Considering that the Kolmogorov-Smirnov test places the least emphasis on the tails of a distribution, its passing results are expected. Despite being regarded as the least powerful test, these results highlight the relationship between tail weight in normality assessments and reinforce the significance of graphical analysis. The normality tests initially indicate a normal distribution for AL and SS samples. To further confirm a normal distribution, graphical methods of analysis are employed.

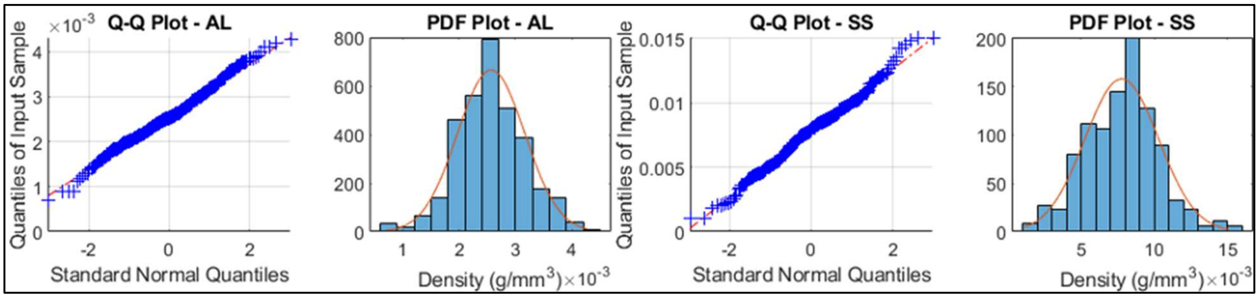

Fig. 8: Plots evaluating the normality of the density distributions

A visual inspection of the quantile-quantile (Q-Q) plot for the AL distribution in Fig. 8 suggests that the data is approximately normal. However, it is noteworthy that the actual count of fragments with densities near the sample mean significantly exceeds the expected count based on a normal distribution.

For SS fragments, Fig. 8 shows how the Q-Q plot deviates significantly at the tail ends of the distribution. After this observation, it is evident why some normality tests failed. The histogram appears to show two modes but still outlines a normal distribution.

4.1.2 Distribution Analysis

The density distribution of SS fragments appears to demonstrate a bimodal pattern, with peaks observed at approximately 5.5 g/cm^3 and 8.5 g/cm^3. This bimodal trend is also apparent in the density histogram for unclassified metals. The observed variability in density cannot be explained by the different types of SS metals (i.e., 304, 316) as they have density ranges of 7.8 g/cm^3 to 8.0 g/cm^3. Instead, several SS-labeled fragments with densities between 4.9 g/cm^3 and 6.1 g/cm^3 are multi-material fragments with SS as the primary material, attached to another metal. This is a consequence of the assessment procedure, which allows for only a single METAL label per fragment, an assumption carried forward by subsequent operators when adding a new revision. Additionally, some of the fragments had foam attached or they were thin, bent plates containing gaps which artificially increased volume. The mode at 8.5 g/cm^3 is notably higher than the maximum feasible density of SS metals. A minor subset of SS fragments with densities exceeding 8.0 g/cm^3 revealed that the underestimation in volume can be traced back to segmentation errors due to specularities.

The mean and median density values for AL fragments are less than the minimum density observed across all AL alloys used in the composition of the satellite. This suggests a systematic overestimation of the actual volume of most AL fragments. Assuming a normal distribution, the real density of AL fragments falls outside the 99% confidence interval of the sample mean, further corroborating the bias towards overestimation of volume.

Nonetheless, 38% of AL fragments showed underestimated volume (i.e., density greater than 2.7 g/cm^3). Of these fragments, calibration errors accounted for 33.3% of the discrepancies, while segmentation issues, such as green foam attached or specularities, affected 21.1% of samples. Misclassifications during assessment, meaning samples composed of multiple materials or entirely different metals, make up 12.1% of the cases. In 9.1% of instances, the fragments seemed devoid of cavities, and their models closely resembled their actual shape, with the calculated density deviating by no more than 2% from the closest feasible density. For the remainder 24.4% of cases, the reason could not be pinpointed due to a lack of adequate data, including absent silhouettes, 3D models, or calibration files.

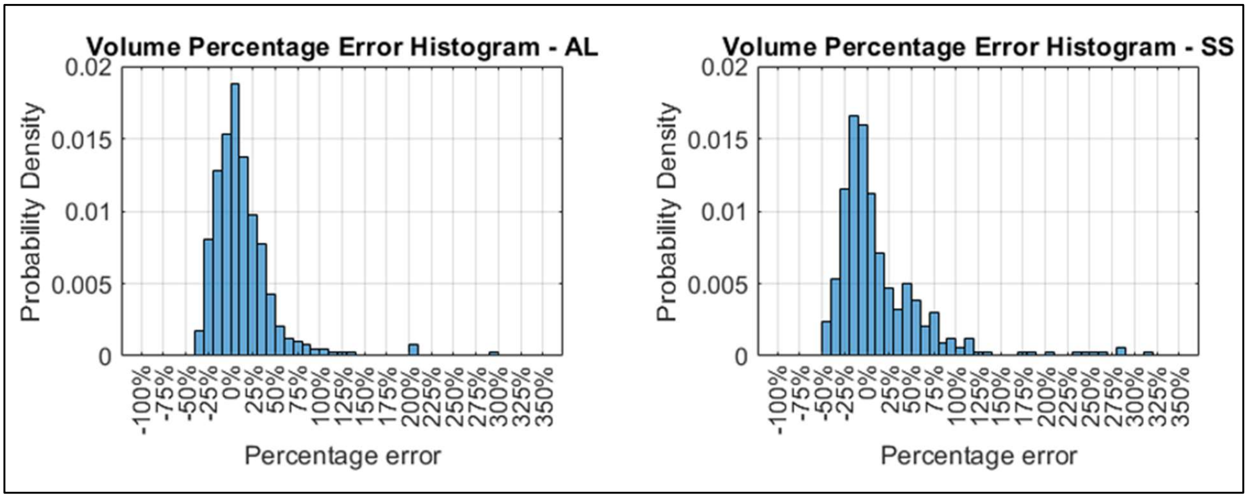

Fig. 9: Histogram showing the distribution of relative errors in volume

The maximum underestimation of volume is no larger than 50%. For AL fragments, the mean absolute percentage error in volume stands at 23%, while it is 36% for SS fragments. The 90% coverage intervals for these volume percentage error distributions are (-26%, 66%) for AL and (-35%, 113%) for SS. For the 95% coverage intervals, these widen to (-29%, 95%) for AL and (-39%, 232%) for SS.

5. CONCLUSION

The present investigation has detailed the various ways in which different error sources influence volume measurements, and consequently, bulk density estimations of actual DebriSat fragments. It has been demonstrated that the well-known overestimation of volume due to silhouette-based shape reconstruction from space carving - assuming accurate silhouettes and well-calibrated cameras - is not the overwhelmingly dominant source of error. Instead, calibration and segmentation errors are sufficiently significant, leading to noticeable effects on the reconstructed volume.

The density distributions of AL and SS fragments demonstrate the tendency of volume overestimations in AL fragments and the apparent density discrepancies with SS densities due to multi-material compositions and fragment specularity. Although the density distribution of AL fragments implies normality through the passing of statistical tests and graphical analysis, the density distribution of SS fragments may not perfectly fit a normal distribution, as the observed data suggests a more complex distribution. Nonetheless, new estimates have been provided that more accurately describe errors in volume and density.

The current study establishes a foundation and highlights the need for more refined error analysis of the DebriSat 3D imaging system. We have demonstrated that calibration errors cannot be overlooked and that significant improvements in overall volume accuracy could be achieved through enhancements in the calibration and segmentation processes. Although this preliminary analysis briefly addressed the shape of fragments, it was not included in the statistical analysis. Future studies could focus on error characterization that accounts for fragment shape. Additionally, further work is required to mitigate algorithmic errors identified in the present study.

REFERENCES

[1] J. Murray, H. Cowardin, J.-C. Liou, M. Sorge, N. Fitz-Coy and T. Huynh, "Analysis of the DebriSat Fragments and Comparison to the NASA Standard Satellite Breakup Model," *First International Orbital Debris Conference*, 2019.

[2] H. Cowardin, C. Cruz, J. Murray, J. Seago, A. Manis, D. Gates, J. Reyes and J. Opiela, "Updates on the DebriSat hypervelocity experiment and characterization of fragments in support of environmental models," *International Journal of Impact Engineering,* 180, 2023.

[3] S. Allen and N. Fitz-Coy, "DebriSat fragment characterization: Quality assurance," *Journal of Space Safety Engineering,* 7(3):235-241, 2020.

[4] J.-C. Liou, S. Clark, N. Fitz-Coy, T. Huynh, J. Opiela, M. Polk, B. Roebuck, R. Rushing, M. Sorge and M. Werremeyer, "DebriSat – A Planned Laboratory-Based Impact Experiment for Breakup Fragment Characterization," *6th European Conference on Space Debris,* 2013.

[5] E. Campa, R. Carrasquilla and N. Fitz-Coy, "ANALYSIS OF DEBRISAT DATA COLLECTION AND PROCEDURES," *Advanced Maui Optical and Space Surveillance Technologies Conference,* 2023.

[6] D. C. Scheider, "Visual Hull," in *Computer Vision*, Boston, MA, Springer, 866-869, 2014, https://doi.org/10.1007/978-0-387-31439-6_211.

[7] A. Laurentini, "The Visual Hull Concept for Silhouette-Based Image Understanding," *IEEE Transactions on Pattern Analysis and Machine Intelligence,* 16(2):150-162, 1994.

[8] B. Shiotani, "Project Life-Cycle and Implementation for a Class of Small Satellites," Ph.D. dissertation, Dept. Mech. Eng., University of Florida, 2018.

[9] C. Carrasquilla, S. Cettei, N. Sutcliffe, N. Fitz-Coy, "From Fragment to 3D Model - Imaging DebriSat Fragments," *20th IAA Symposium on Space Debris*, 2022.

[10] N. Razali and Y. Wah, "Power comparisons of Shapiro-Wilk, Kolmogorov-Smirnov, Lilliefors and Anderson-Darling tests," *Journal of Statistical Modeling and Analytics,* 2(1):21-33, 2011.

[11] A. Loy, L. Follett and H. Hofmann, "Variations of Q-Q Plots: The Power of Our Eyes!," *The American Statistician,* 73(2):202-214, 2019.